Corrosion Science 227 (2024) 111698

Contents lists available at ScienceDirect

Corrosion Science

journal homepage: www.elsevier.com/locate/corsci

Corrosion behavior assessment of an Al-Cu alloy manufactured via laser powder bed fusion

Sergio Lorenzi [a,b,*], Alessandro Carrozza [a,b], Marina Cabrini [a,b], Lorenzo Nani [a,b], Francesco Andreatta [b,c], Eero Virtanen [d], Tommaso Tirelli [e], Tommaso Pastore [a,b]

[a] Department of Engineering and Applied Sciences, University of Bergamo, Dalmine, Italy
[b] National Interuniversity Consortium of Materials Science and Technology (INSTM), Firenze, Italy
[c] Polytechnic Department of Engineering and Architecture, University of Udine, Udine, Italy
[d] Electro Optical Systems (EOS), Turku, Finland
[e] AIDRO Hydraulics & 3D Printing, Taino, Italy

ARTICLE INFO

Keywords:
Additive manufacturing
Aluminium
Al-Cu
Corrosion
Heat treatments
AFM

ABSTRACT

Additively manufactured Aluminum-Copper alloys are attracting interest because of their high tensile strength. Nevertheless, the presence of Cu strongly affects the corrosion performances. In this work, the corrosion behavior of an innovative laser powder bed fusion-processed 2139 alloy was investigated, and its corrosion performances were compared to the well-consolidated AlSi10Mg alloy, as well as the parent wrought alloy. Electrochemical, Kelvin probe microscopy and intergranular corrosion tests were performed. The unique corrosion morphology at melt pool boundaries are presented and discussed alongside with the effect of surface finishing and heat treatments.

1. Introduction

Additive manufacturing (AM) technologies are quickly becoming an established industrial reality, as confirmed by the exponentially growing number of papers published on this subject [1,2]. Laser powder bed fusion (LPBF or PBF-LB) is an AM technique that deploys a layer-by-layer approach to selectively melt a powder layer, using a laser as a heat source. This process results in very high cooling rates, thus providing unique out-of-equilibrium microstructures and typical defects (e.g., lack of fusion porosities) [3]. Furthermore, microstructural modification via specifically tailored post-processing heat treatments is possible [4]. All these peculiarities are the reason why a strong need for ad hoc standardization in this field is necessary nowadays. In this framework, a crescendo of papers and committees of different standardization bodies for the qualification of AM-processed alloys is evident in recent years [5,6].

Aluminum alloys are very popular materials to be processed via LPBF due to the intricate designs and superior mechanical properties that can be achieved [7,8]. Moreover, AM technologies are economically promising in industries characterized by small production volumes and high costs components. Such as the industrial fields where Al alloys are largely deployed, for example the automotive [9], marine [10] and military [11] sectors. This wide variety of applications results in very different operative environments, thus corrosion types. For this reason, ad hoc qualifications are of great industrial interests in each field. In fact, LPBF-processed Al alloys greatly differ from conventionally processed ones due to the possible insurgence of non-equilibrium phases [12], compositional/microstructural variations between the center and the edge of the melt pool [13], anisotropy [14], possible cellular structures [15] and uneven element distributions [16]. Defects, porosity and residual stress can also influence the corrosion behavior [17].

In LPBF, AlSi10Mg is by far the most studied alloy due to its near-eutectic composition and high castability (effect of Si), allowing to achieve very low porosity values. Notwithstanding this, an increasing number of works in the literature is focusing on other LPBF-processed Al alloys, such as AlSi12Mg [18], AlSi7Mg (A357) [19] and 2024 [20].

Several works dealing with the corrosion behavior assessment of the LPBF-processed AlSi10Mg available in the literature consider a wide range of process parameters, building strategies, surface finishing, heat treatments, test solutions and methodologies [21–23]. Therefore, most results are usually hardly comparable. Nevertheless, it is generally accepted that the corrosion resistance of AM-processed parts is usually

* Corresponding author at: Department of Engineering and Applied Sciences, University of Bergamo, Dalmine, Italy.
E-mail address: sergio.lorenzi@unibg.it (S. Lorenzi).

https://doi.org/10.1016/j.corsci.2023.111698
Received 15 June 2023; Received in revised form 7 November 2023; Accepted 19 November 2023
Available online 22 November 2023

better than in the corresponding cast alloys. This can be observed, for instance, in works from Leon et al. [24] and Fathi et al. [25], where the mass loss and potentiodynamic curves in a NaCl solutions were assessed, respectively.

In general, materials characterized by a good weldability are well suited for LPBF processing. As mentioned before, Al-Si systems are very processable, due to their high castability. However, these alloys provide lower mechanical performance with respect to precipitation hardened alloys [26]. Among this category, the 2XXX series alloys are characterized by a good weldability, thus being promising for AM applications. This is the main reason why LPBF-processed Al-Cu systems are receiving an increasing interest in recent years [27,28]. However, the achievement of the aforementioned high mechanical properties is related to the nucleation of small precipitates, conventionally achieved by generating a dislocation network via deformation of the material after heat treatment. Unfortunately, this is in direct contrast with the near-net shape approach of the LPBF technology. Among the Al-Cu systems, the alloy 2139 is a precipitation-strengthened Al-Cu-Mg-Ag alloy. This material can achieve its peak strength via plate-like Al_2Cu precipitates, that do not require a high dislocation density to form, hence deformation. The precipitation of such strengthening phase is the result of a homogeneous nucleation from nanometric Mg- and Ag-rich co-clusters during the early stages of the aging treatment [29]. In recent years, the AM-processed alloy 2139 is receiving a certain interest in the literature [30–32].

Overall, copper is usually considered as a deleterious alloying element in Al alloys, concerning the corrosion resistance in solutions rich in chlorides [33,34]. For instance, Banu et al. [35] reported that lower pitting potentials are achieved at increasing Cu contents in alkaline, neutral and acid solutions. Román et al. [33] stated that Cu additions result in a decrease in corrosion resistance, due to the increasing number of cathodic sites. Moreover, these authors also reported that large amounts of Al_2Cu might result in an increased susceptibility to intergranular corrosion.

Apart for the existing literature dealing with the effect of Cu in the conventionally processed material, the evaluation of the corrosion behavior of this alloy processed via LPBF is still a gap in the current literature. Therefore, the corrosion behavior assessment of the alloy 2139 produced via LPBF was performed in this work. Both the as-built and heat-treated conditions were considered. Moreover, this material was comparatively analyzed with the well-established LPBF-processed AlSi10Mg alloy and the conventionally hot-worked alloy AA 2139 T351 with similar chemical composition. Electrochemical impedance spectroscopy, potentiodynamic polarization and susceptivity to intergranular corrosion tests were conducted. Additionally, a scanning Kelvin probe force atomic microscope (SKPFM) analysis was also performed to analyze the galvanic effect of the second phases.

2. Experimental

2.1. Specimens fabrication

Cylindrical specimens (15 mm diameter, 5 mm tall) were manufactured using an EOS M290 LPBF machine to process EOS aluminium Al2139AM (alloy 2139) and AlSi10Mg powders, both supplied by EOS GmbH. The powders were characterized by a particle size range of 20–63 μm and 27–76 μm for the 2139 and AlSi10Mg alloys, respectively. The nominal compositions of the additively manufactured alloy powders alongside with the wrought AA 2139 T351 alloy are shown in Table 1.

The fabrication step deployed a heating system that kept the baseplate temperature as high as 165 °C (AlSi10Mg) and 175 °C (2139) throughout the whole process. The cylindrical specimens were built following two different orientations: Z (base perpendicular to the building platform) and XY (base parallel to the building platform).

The additively-manufactured samples were studied in the as-built (AB) and heat-treated (HT) conditions. The alloy 2139 underwent a T4 heat treatment, whilst the alloy AlSi10Mg underwent a T6 heat treatment. The temperatures and cooling means adopted are summarized in Table 2.

2.2. Metallographic investigations

The microstructure of the LPBF-processed specimens in the AB and HT conditions was evaluated on metallographic cross-sections, parallel to the building direction (Z). By doing so, assessing possible differences induced by the different laser tracks/layers was possible. The microstructure of the wrought AA 2139 was evaluated in the cross sections parallel to the rolling direction. In order to obtain the samples for micrographic analyses, some cylindrical specimens were mechanically ground with SiC papers up to a 4000 grit, then polished with a 1 μm diamond suspension. The microstructures were highlighted via chemical etching, using a Keller reagent. Microstructural investigations were performed using a Keyence VHX-7100 digital-optical microscope (OM) and a Gemini Sigma 300 field emission scanning electron microscope (FESEM), equipped with an Oxford x-act probe for energy-dispersive X-ray spectroscopy (EDS).

2.3. Corrosion behavior assessment

2.3.1. Electrochemical tests

The cylindrical specimens were considered for electrochemical testing. For this specific experimental campaign, the effect of surface finishing was considered alongside the influence of the heat treatment. The specimens that did not underwent polishing operations were labelled as not polished (NP), whilst the other were mechanically polished (MP).

Electrochemical impedance spectroscopy (EIS) and potentiodynamic polarization (PD) tests were performed with a Ivium CompactStat and a Metrohm Autolab potentiostats, a 1 L glass cell (according to ASTM G5–82), two graphite electrodes and a saturated calomel reference electrode (SCE) placed in a Luggin probe. The cylindrical samples were

Table 2
Heat treatment parameters.

Heat treatment	Solubilization temperature	Aging temperature
T4 (2139)	490 °C, then water quenching	25 °C
T6 (AlSi10Mg)	530 °C, then water quenching	160 °C

The T4 heat treatment was selected for mechanical properties improvement. In fact, this post-processing route resulted in an increase from 115 to 157 Vickers hardness in the alloy 2139.

Table 1
Chemical composition (wt%) of the investigated alloys.

Element (wt%)	Al	Cu	Mg	Ag	Mn	Zn	Si	Fe	Cr	V	Other
2139[1]	bal.	4.5 ÷ 5.5	> 0.8	0.15 ÷ 0.6	0.2 ÷ 0.6	< 0.25	< 0.1	< 0.15	< 0.05	< 0.05	< 4
AlSi10Mg[2]	bal.	< 0.01	0.36	-	< 0.01	0.01	10.3	0.14	-	-	< 0.15
AA 2139 T351[3]	bal.	4.56	0.41	0.40	0.24	-	-	0.09	-	-	-

[1] As provided by the supplier
[2] Measured by means of inductively coupled plasma atomic emission spectrometry
[3] as reported by Balbo et al. [36]

fitted inside a PTFE sample holder that exposed to the test solution a surface of 0.785 cm^2. The MP specimens were mechanically ground with SiC papers up to a 4000 grit, polished with a 1 μm diamond paste, degreased in acetone and then passivated in a dryer for at least 48 h at room temperature.

EIS and PD tests were performed at room temperature (23 ± 2 °C) in an aerated solution containing 1 g/L sodium chloride and 41.18 g/L sodium sulphate.

The EIS tests included a first phase of stabilization for 3600 s and monitoring of the open circuit potential (OCP). Then, the spectrum was detected with a sinusoidal polarization of 10 mV of amplitude in a frequency range between 0.01 and 40,000 Hz, collecting 5 frequency values for each decade. After the EIS tests, the OCPs were re-stabilized and monitored for 300 s, then the PD tests started. These were performed with a potential scanning speed of 10 mV/minute, starting from − 10 mV with respect to the OCP, up to an anodic density of current equal to 1 mA/cm^2.

At least two specimens were tested for each condition.

2.3.2. Volta potential measurements

The as-built (AB) and T4 LPBF 2139 alloy samples were investigated using a scanning Kelvin probe force microscope (Nanoscope III multimode atomic force microscope) to investigate the distribution of the surface potential. These samples were characterized after polishing (up to 1 μm surface finish). Topographic and surface potential maps were obtained employing n^+-silicon tips coated with $PtIr_5$. Maps with variable sizes ranging from 100 μm x 100–50 μm x 50 μm were recorded with a scan frequency of 0.1 Hz. The surface potential maps (Volta potential) were measured in lift mode with a scan height of 100 nm.

2.3.3. Susceptibility to intergranular corrosion test

Susceptibility to selective corrosion tests were performed in accordance to the EN ISO 11846 standard (Method B). Prior to the tests, the specimens were mechanically ground with SiC papers up to a 2400 grit. The initial specimen sizes (diameter and height) were measured with a Vernier caliper. The samples were then degreased with acetone, immersed for 3.5 min in a sodium hydroxide solution (8% in weight at 55 ± 2 °C), rinsed in water, immersed for 2 min in concentrated nitric acid, rinsed in distilled water and dried. The specimens were subsequently immersed in the test solution, containing 30 g/L sodium chloride and 10 mL/L concentrated hydrochloric acid, at room temperature for 24 h. During the tests, the temperature of the test solution was held within a range of 21–25 °C. After immersion, the samples were rinsed in distilled water and dried. Corrosion products were removed with a non-metallic brush, while rinsed in distilled water. The samples were then immersed in an ultrasonic bath of acetone, and subsequently allowed to dry. The mass loss during the test was obtained as the difference between the initial mass of the specimen and that measured after the immersion period. Each weighing has been repeated three times. At the end of the test, a metallographic section perpendicular to the exposed surface was investigated to assess the presence and depth of the attacks.

3. Results and discussion

3.1. Analysis of the microstructure

The LPBF-processed alloy 2139 specimens in the AB condition were characterized by the typical melt pool microstructure (Fig. 1a), given by the interaction of multiple laser tracks during the manufacturing process. Microstructural coarsening was evident in correspondence of the border of the melt pool with respect to its center (Fig. 1b, c). The AB condition was characterized by a matrix of α-Al cells, decorated by a discontinuous layer of Al_2Cu (Fig. 1d) (≃ 11.5% in volume). This is confirmed by the EDS maps (Fig. 1e) and the XRD patterns (Fig. 2). This particular arrangement of the second phase is related to the very high cooling rate achieved during the LPBF process, as confirmed by similar findings from Elambasseril et al. [32], who also encountered a similar structure in the atomized alloy 2139 powders. The morphology of the precipitates changed after the T4 heat treatment, resulting in the formation of bulky particles (Fig. 1f) (≃ 8.5% in volume). These were still Al_2Cu, as established by the EDS maps (Fig. 1g) and XRD tests (Fig. 2). The melt pool macrostructure disappeared completely after the heat treatment.

The benchmark LPBF-processed AlSi10Mg alloy was characterized by the presence of the typical melt pool microstructure as well (Fig. 3a,b, c) with the typical Si-rich network surrounding the α-Al matrix (Fig. 3d, e), as assessed in several works in the literature [37,38]. However,

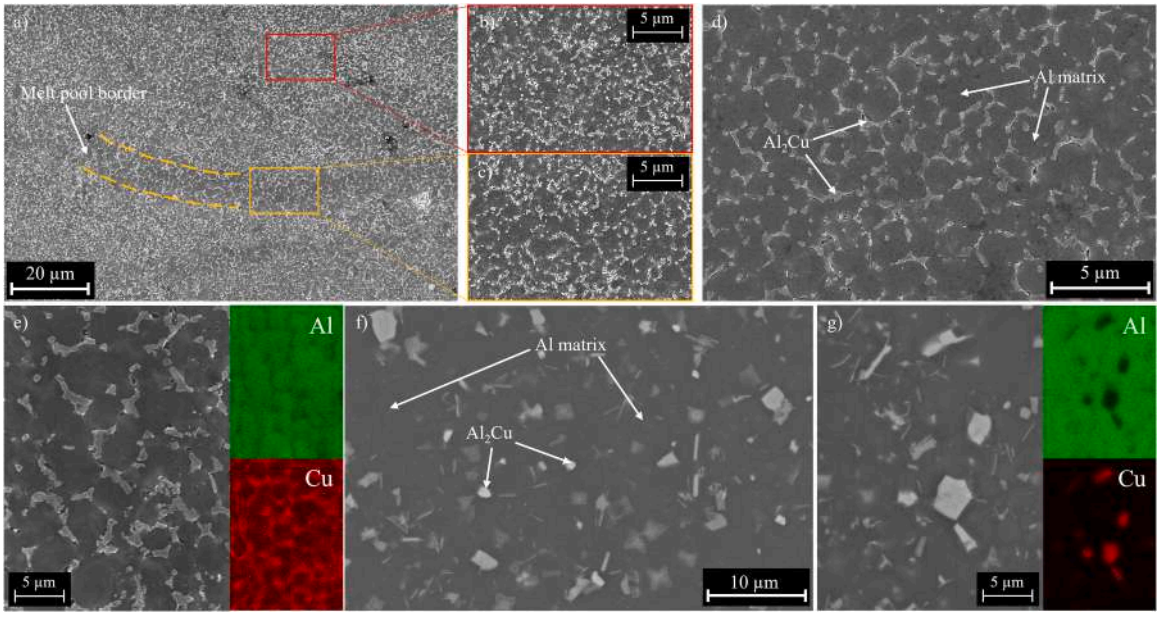

Fig. 1. Low-magnification FESEM micrograph of the alloy 2139 as-built specimens (a) with highlighted melt pool central (b) and border (c) regions. Second phase morphology in the as-built material (d) and relative main element distribution EDS maps (e). SEM micrograph of the alloy 2139 after the T4 heat treatment (f) and relative main element distribution maps (g).

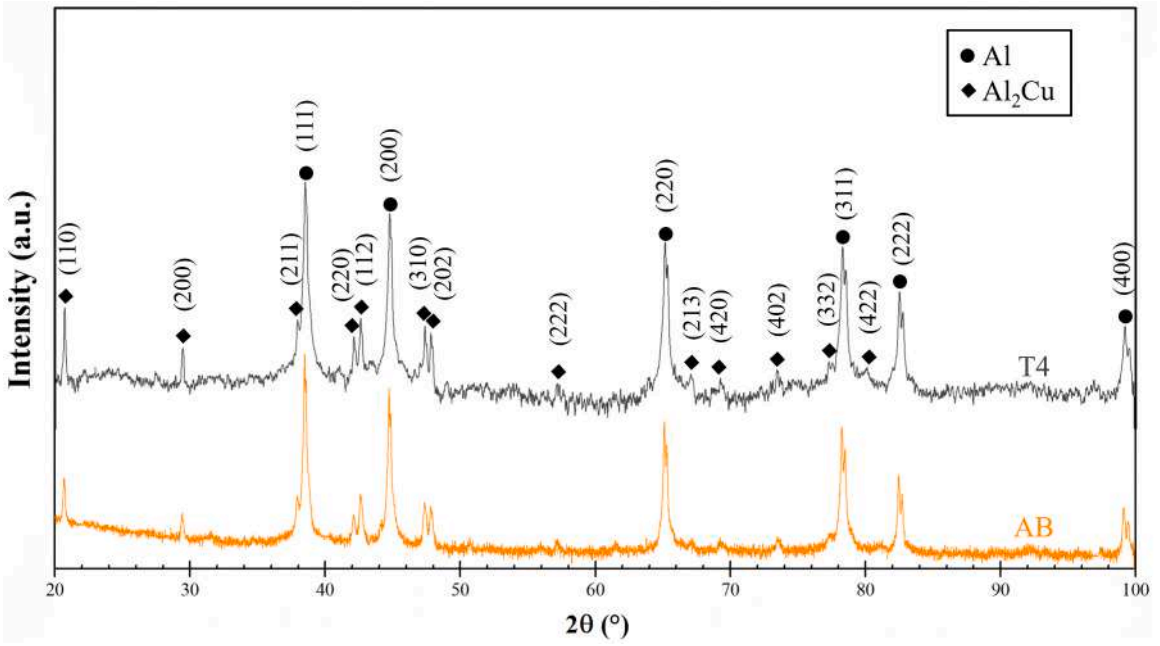

Fig. 2. XRD pattern of the alloy 2139 in the AB condition and after T4 heat treatment.

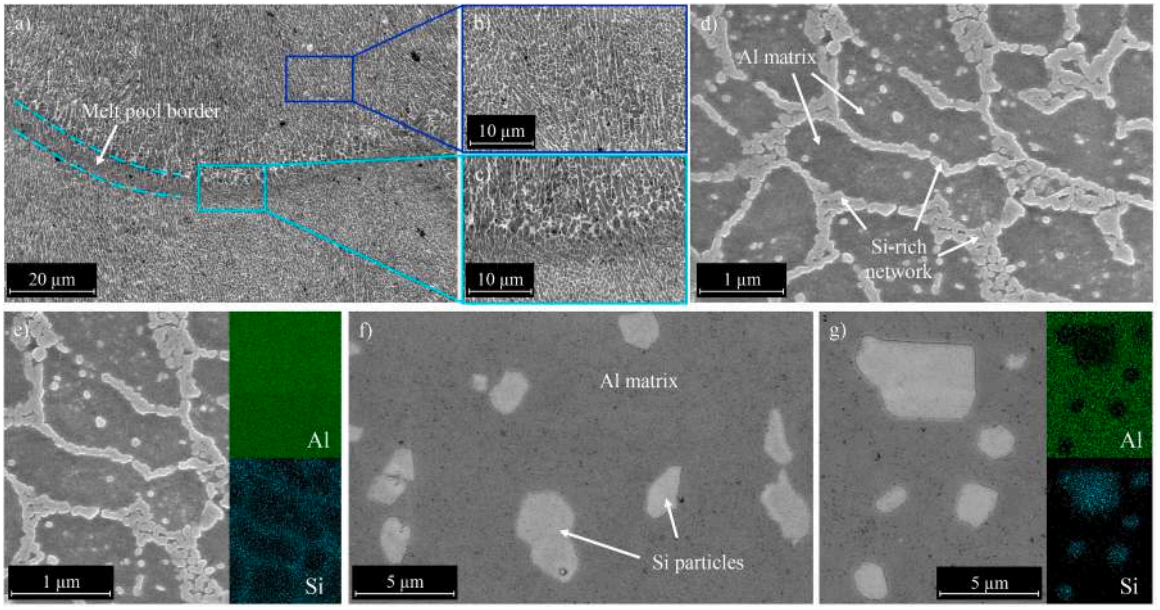

Fig. 3. Low-magnification FESEM micrograph of the alloy LPBF AlSi10Mg as-built specimens (a) with highlighted melt pool central (b) and border (c) regions. Second phase morphology in the as-built material (d) and relative main element distribution EDS maps (e). SEM micrograph of the alloy AlSi10Mg after the T6 heat treatment (f) and relative main element distribution maps (g).

coarsening of the network and subsequent precipitation of Si-rich particles occurred due to the high platform temperature adopted during the process [39]. After the T6 heat treatment, the coalescence of the Si particles was observed in conjunction with the complete disruption of the Si-rich network and the melt pool macrostructure (Fig. 3f,g).

The wrought AA 2139 alloy showed a microstructure with elongated grains along the rolling direction (Fig. 4a), as already assessed in several literature studies [36,40]. The presence of coarse, copper-rich second phases is also evident, as showed by higher magnification micrographs and related EDS maps (Fig. 4b).

3.2. Corrosion behavior assessment

In a previous paper [41], the authors found for the AlSi10Mg a linear relationship between breakdown potential and chloride concentration followed the mechanism proposed by McCafferty [42]. A practical active behavior increasing with chloride activity was observed. The electrochemical tests in this work were carried out in the lowest chloride concentration tested in [41] in order to compare the two LPBF-processed Al alloys, having the typical melt pool microstructure. The results obtained for the LPBF 2139 were compared also with their commercial hot rolled counterpart AA 2139 T351.

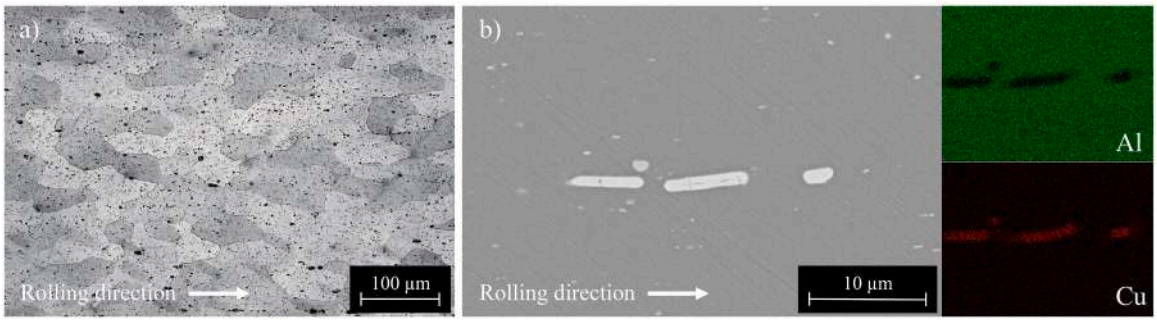

Fig. 4. Low-magnification OM micrograph of the wrought AA 2139 T351 specimens (a) and FESEM micrograph highlighting second phases morphology (b) and main element distribution EDS maps.

3.2.1. As-built specimens

The OCP values obtained at the beginning of the electrochemical investigation of the specimens are reported in Table 3. The LPBF 2139 alloy exhibited a higher OCP than LPBF AlSi10Mg, due to the higher nobility of Cu [43]. Furthermore, surface finishing did not seem to affect the OCP, obtaining similar values for NP and MP specimens of each alloy.

Local alkalinization destabilizes the aluminium passive film, resulting in ITS breakage even at very low chloride concentrations. The oxygen reduction process takes place preferentially on the noblest intermetallic precipitates with lower overvoltage for oxygen electrochemical reaction (OER) [44]. This leads to the preferential corrosion of the Al-matrix adjacent to the precipitates, as demonstrated in numerous works on Al-Cu alloys. According to Birbilis and Buchheit [45], Al_2Cu corrosion potential in 0.01 M solution is − 0.592 V vs SCE is similar to the values obtained for the LPBF 2139 alloy. Conversely, Si corrosion potential is − 0.450 V vs SCE. In the case of the LPBF-processed AlSi10Mg alloy, the silicon is partially solubilized in the aluminum matrix, with very small precipitates dispersed evenly within the melt pool surrounding the crystals of α-Al matrix, whilst segregating into idiomorphic crystals at the melt pool border. These precipitates do not influence the OCP potential, probably due to the high over potential for OER.

Considering NP specimens, the LPBF 2139 alloy provided Bode diagrams characterized by two separate and well-defined phase constants, as shown in Fig. 5a. These results are in good agreement with other studies on traditional Al-Cu alloys. For instance, Moreto et al. [46] assessed the electrochemical behavior of an AA2024 alloy in chloride-rich environments. Conversely, the AlSi10Mg alloy evidenced the presence of a very small secondary peak at low frequencies in the NP condition (Fig. 5b). Following the mechanical polishing, the oxide film generated during the production process was removed and replaced by the oxide formed under controlled conditions. This layer is known to be more protective than the one produced during LPBF processing. Hence, the disappearance of the low-frequency peak was encountered, due to the suppression of the corrosive processes. The enlargement of the phase curve in the MP AlSi10Mg specimens was associated with a higher modulus. In the LPBF 2139 alloy the effect of the microstructure was still predominant over the surface finishing, obtaining similar spectra in the NP and MP specimens. On the contrary, MP LPBF AlSi10Mg specimens exhibited low frequencies modulus values higher by an order of magnitude with respect to NP samples. Therefore, a highly protective and stable oxide film with high polarization resistance values was generated in the MP AlSi10Mg alloy.

In a previous work on the corrosion behavior of the LPBF AlSi10Mg alloy [47], the presence of two phase constants was attributed to the concomitance of three separate processes: the cathodic behavior of the nobler second phases, the active dissolution of the α-Al matrix adjacent to the cathodic particles and the presence of the passive film on the α-Al matrix distant from the cathodic particles. According to this work, the EIS spectra obtained were approximated with an equivalent circuit following the Voigt model [48], as shown in Fig. 5, in which the diffusive contribute reported in [47] has been removed, since the EIS spectra were recorded only after 1 h immersion, there was therefore no time for the localized attack to deeply propagate. This equivalent circuit is composed of resistors (R) and constant-phase elements (CPE). According to this model, the results obtained can be represented through three elements placed in series: a resistance of the bulk electrolyte (R1), a parallel CPE2-R2 (with low frequency response) representing corrosive processes and a second parallel CPE3-R3 (with high frequency response) representing the presence of the oxide film (Fig. 6). Therefore, the modulus evaluated at low frequency is indicative of the polarization resistance.

In the case of LPBF AlSi10Mg alloy, the cathodic second phases were idiomorphic silicon crystals, characterized by a mild cathodic action due to the high overvoltage of the oxygen reduction process [49,50]. Copper-rich precipitates in 2139 alloy turned out to be more efficient cathodes. This phenomenon led to a very fast trigger of the corrosion phenomena in the adjacent matrix, as demonstrated by the lower impedance modulus values at low frequencies (Table 4).

These assumptions were confirmed by the potentiodynamic polarization curves (Fig. 7) that showed for both the LPBF-processed alloys a fully active behavior in the NP specimens. Additionally, no significant variations were inducted by the mechanical polishing in the LPBF 2139 alloy (Fig. 7a). In fact, the cathodic activation effect operated by the precipitates overcame the improvement of the passive film. Conversely, the removal of the LPBF-generated passive film and its relative substitution with a better-performing one resulted in an improved behavior towards localized corrosion initiation in the LPBF AlSi10Mg specimens, that exhibited pronounced passive traits (Fig. 7b). The breakdown potentials are reported in Table 5; the values of the breakdown potential of

Table 3
Open circuit potentials of the tested specimens.

Alloy	Surface condition	Condition	OCP vs SCE (mV)
LPBF 2139	NP	AB	- 584 ± 14
		T4	- 477 ± 8
	MP	AB	- 591 ± 15
		T4	- 473 ± 5
LPBF AlSi10Mg	NP	AB	- 669 ± 4
		T6	- 598 ± 10
	MP	AB	- 670 ± 22
		T6	- 627 ± 30
Wrought AA 2139	MP	T351	- 513 ± 15

The OCP values showed an initial passive behavior for both 2139 and AlSi10Mg alloys. At this step, the cathodic process is the oxygen reduction according to the reaction:

$$\frac{1}{2}O_2 + H_2O + 2e^- \rightarrow 2OH^- \quad (1)$$

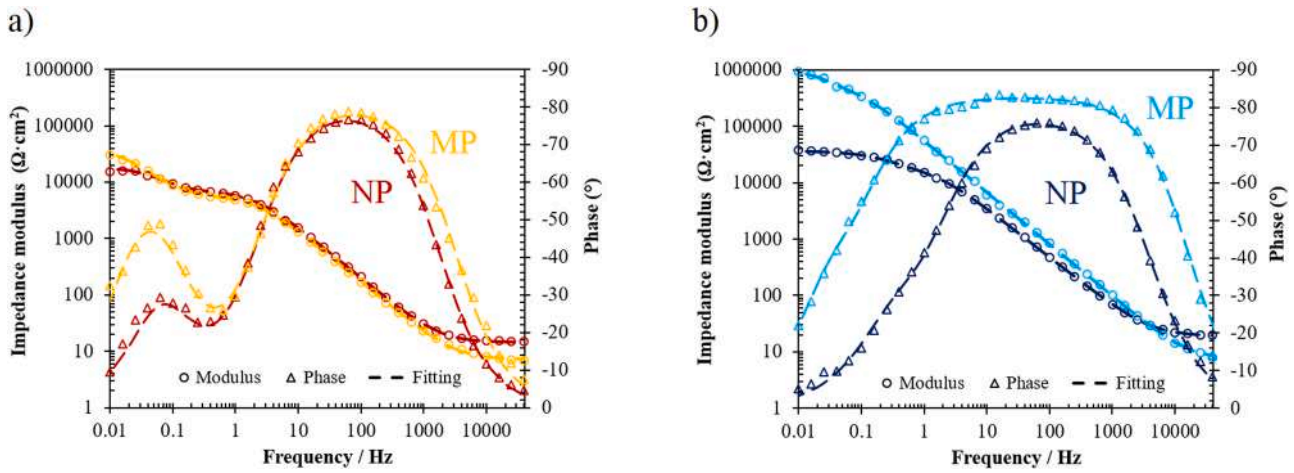

Fig. 5. EIS spectra of 2139 (a) and AlSi10Mg (b) AB specimens.

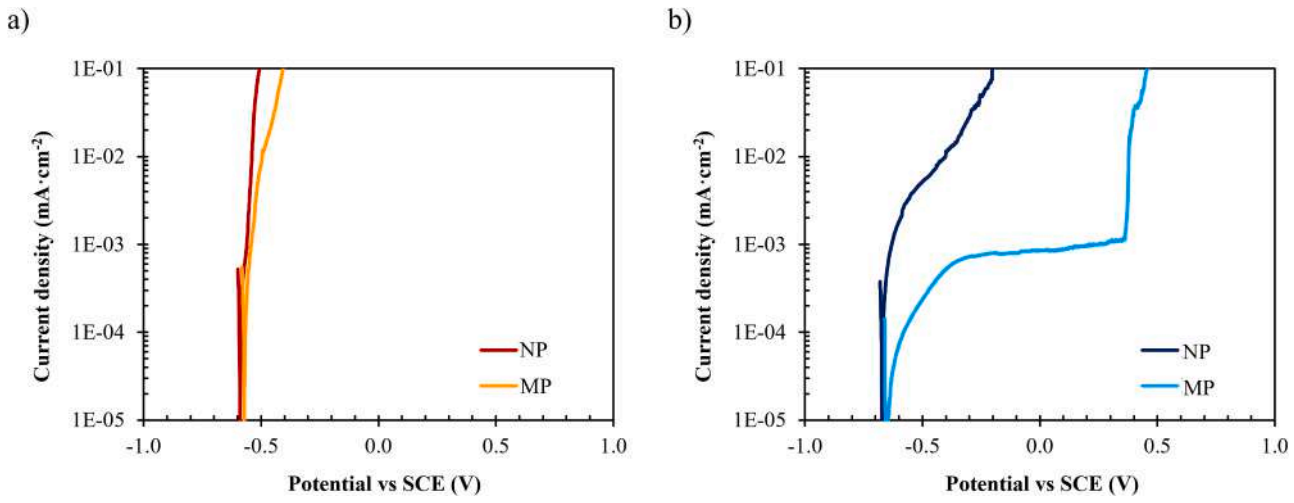

Fig. 6. Voigt equivalent circuit with two time constants.

Table 4
Fitting parameters and low frequencies modulus of the tested specimens.

Alloy	Surface condition	Condition	R_1 / Ω·cm²	R_2 / kΩ·cm²	CPE_2 / μF·cm^{-2}	n_2	R_3 / kΩ·cm²	CPE_3 / μF·cm^{-2}	n_3	$\|Z\|_{0.01\ Hz}$ / kΩ·cm²
LPBF 2139	NP	AB	14 ± 1	29 ± 18	291 ± 42	0.86 ± 0.10	5 ± 1	36 ± 21	0.95 ± 0.05	22 ± 7
		T4	18 ± 1	9 ± 2	392 ± 10	0.90 ± 0.01	5 ± 1	24 ± 1	0.92 ± 0.01	15 ± 1
	MP	AB	18 ± 1	28 ± 8	323 ± 55	0.97 ± 0.03	5 ± 1	20 ± 1	0.92 ± 0.01	29 ± 9
		T4	8 ± 2	47 ± 8	83 ± 5	0.90 ± 0.09	10 ± 1	11 ± 1	0.95 ± 0.03	57 ± 7
LPBF AlSi10Mg	NP	AB	21 ± 2	17 ± 9	136 ± 95	0.73 ± 0.09	7 ± 4	16 ± 7	0.86 ± 0.04	23 ± 14
		T6	13 ± 1	65 ± 7	183 ± 49	0.89 ± 0.11	28 ± 16	15 ± 7	0.92 ± 0.01	66 ± 28
	MP	AB	13 ± 5	710 ± 94	11 ± 2	0.93 ± 0.01	266 ± 14	7 ± 2	0.91 ± 0.01	839 ± 78
		T6	8 ± 2	546 ± 26	7 ± 1	0.95 ± 0.05	235 ± 103	7 ± 2	0.91 ± 0.01	772 ± 67
Wrought AA 2139	MP	T 351	8 ± 1	28 ± 1	277 ± 4	0.92 ± 0.01	7 ± 1	12 ± 1	0.89 ± 0.01	28 ± 1

the AlSi10Mg MP specimens are quite scattered owing to the emerging porosity, but significatively higher than the break down potential of the LPBF 2139 MP.

The cathodic effect of the second phases in alloy LPBF 2139 was also confirmed by the corrosion current densities obtained by extrapolating the Tafel plots from the potentiodynamic polarization curves. Tafel lines

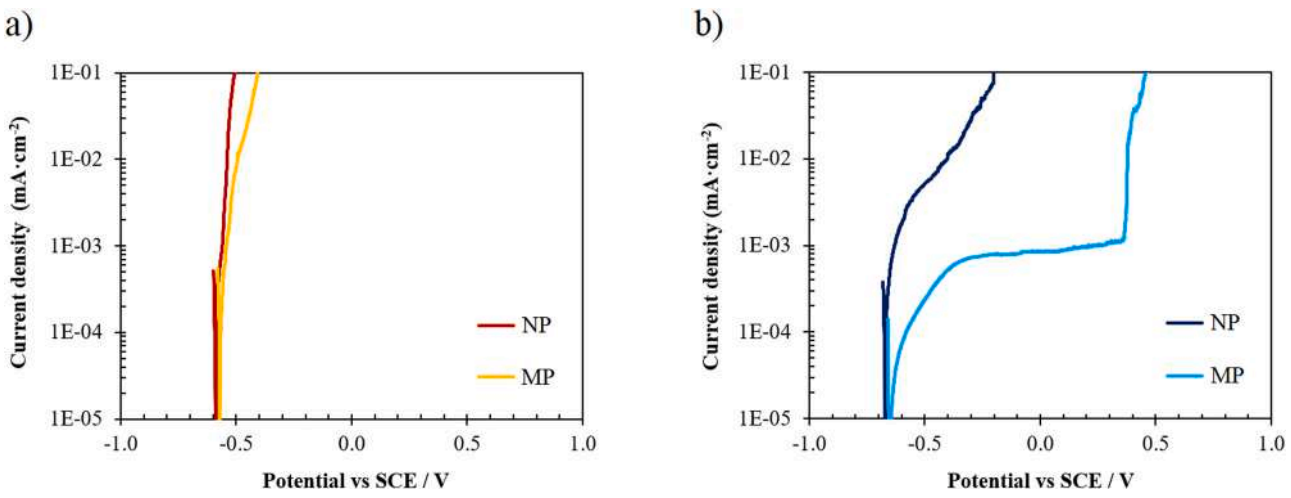

Fig. 7. AB LPBF 2139 (a) and AB LPBF AlSi10Mg (b) alloys potentiodynamic polarization curves.

Table 5
Corrosion current densities and breakdown potentials of the tested specimens.

Alloy	Surface condtion	Condition	i_{corr} ($\mu A \cdot cm^{-2}$)	E_{bd} vs SCE (mV)[a]
2139	NP	AB	6.311 ± 2.813	- 584 ± 14
		T4	7.319 ± 2.314	- 477 ± 8
	MP	AB	0.431 ± 0.041	- 591 ± 15
		T4	0.270 ± 0.010	- 473 ± 5
AlSi10Mg	NP	AB	0.789 ± 0.481	- 669 ± 4
		T6	0.463 ± 0.162	- 598 ± 10
	MP	AB	0.062 ± 0.008	+ 225 ± 92
		T6	0.062 ± 0.005	- 128 ± 152
Wrought AA 2139	MP	T351	0.423 ± 0.074	- 513 ± 15

[a] For active specimens the OCP was considered as breakdown potential.

were extrapolated from an overpotential 100 mV higher than the OCP, as reported in Table 5. The alloy LPBF 2139 specimens provided a corrosion current density about an order of magnitude greater than alloy AlSi10Mg if the same surface condition is considered. In addition, it is evident that the surface finishing had a significant effect on the corrosion current densities developed, with NP specimens showing higher corrosion rates than MP counterparts, confirming the poor protection offered by the oxide film formed during processing. These results are in agreement with the results obtained from the EIS tests, as the corrosion current density decreases with increasing impedance modulus at low frequencies.

The susceptibility to intergranular corrosion tests allowed to further assess the detrimental effect of Cu in the alloy LPBF 2139, testified by the significantly higher corrosion rate encountered in the AB specimens (Table 6). In fact, the alloy LPBF 2139 provided a corrosion rate an order of magnitude higher than the LPBF AlSi10Mg alloy.

The investigation of the selective attack paths in the cross-sections of the specimens that underwent this test (Fig. 8, Table 6) highlighted a predisposition to this corrosion mechanism in the specimens of both alloys. In fact, the melt pool boundaries provided a preferential path to the advancement of intergranular attacks, which macroscopically assumed an inter-melt pool morphology (Fig. 8a, d). In particular, the alloy LPBF 2139 specimens showed several attacks on the entire surface, following evident preferential paths located at the border of the melt pools (Fig. 8b), where coarsening of the Al_2Cu structure occurs (Fig. 1b, c). The selective attack proceeded by clear preferential dissolution of the Al matrix, due to the galvanic effect of Cu. This behavior is confirmed by Fig. 8c, where the residual Al_2Cu network was still present in the corrosion crack. Furthermore, an EDS map of a corroded area (Fig. 9) confirmed the dissolution of the Al matrix, due to the corrosion product being significantly rich in Cu and O. The detrimental effect of Cu in alloy LPBF 2139 was further testified by the significantly higher corrosion rate. Moreover, the attack undermined abundant parts of the material (grain dropping), resulting in a mass loss of the specimens far greater than the dissolved metal. This phenomenon was particularly noticeable due to the test solution showing significant metal deposits at the end of the test.

The preferential corrosion of the melt pool boundary has been extensively studied for alloy LPBF AlSi10Mg [50,51]. SKPFM measurements have shown that the differences in terms of potential between the α-Al matrix and the silicon precipitates at the edge of the melt pool are higher than at the center of it [52]. This was attributed to the silicon supersaturation of the matrix at the center of the melt pool due to the higher local cooling rate. The clear presence of a residual Si-rich

Table 6
Outcome of the susceptibility to intergranular corrosion tests on the 2139 and AlSi10Mg alloys, evaluated in compliance with ISO 11846.

Alloy	Condition	Exposed surface (cm^2)	Mass loss (mg)	v_{corr} ($mg \cdot dm^{-2} \cdot day^{-1}$)	Average depth (μm)	Maximum depth (μm)	Attack linear density (mm^{-1})
2139	AB	5.65 ± 0.21	240 ± 50	4220 ± 789	248 ± 88	641	4.4
	T4	5.65 ± 0.21	20 ± 9.5	357 ± 165	157 ± 49	182	0.8
AlSi10Mg	AB	5.50 ± 0.01	29 ± 14.4	525 ± 261	539 ± 271	899	0.5
	T6	5.57 ± 0.12	12 ± 2.1	209 ± 35	-[1]	-[1]	-[1]
Wrought AA 2139	T 351	5.40 ± 0.03	140 ± 5.3	2590 ± 110	278 ± 88[2]	503[2]	11.1[2]

1Not reported due to the different corrosion mechanism highlighted
2Attack depths evaluated along the rolling direction

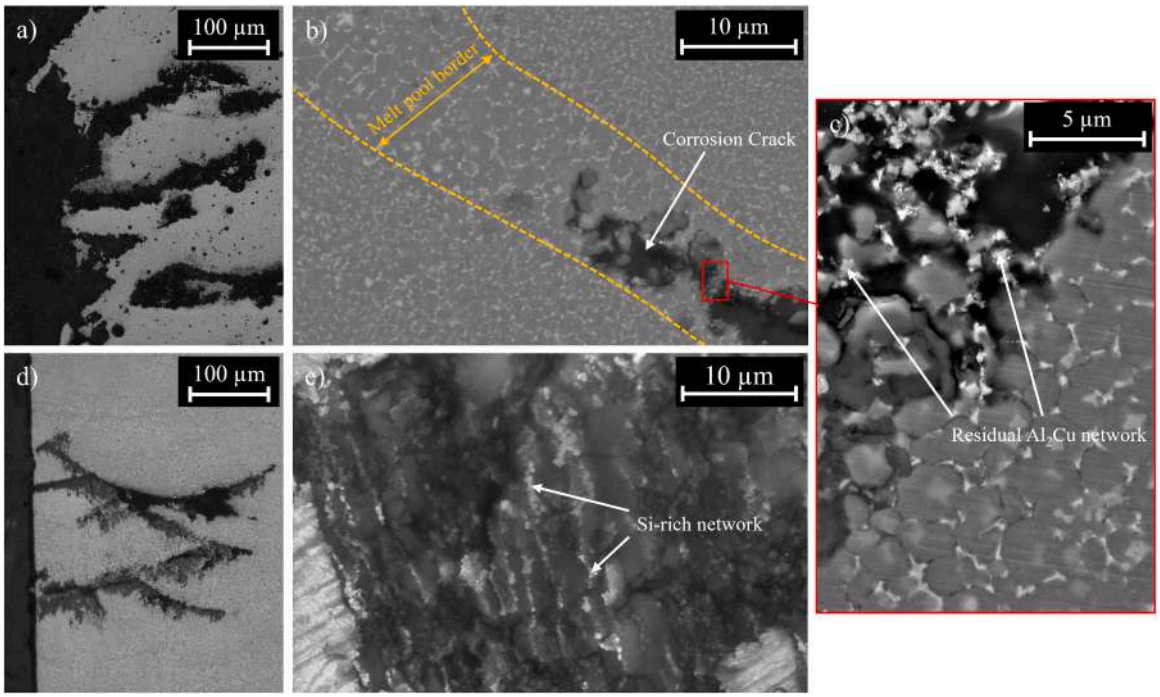

Fig. 8. Morphology of the selective attack at the edge of the specimens (a,d), relative propagation (b,e) and inset of the corroded area (c) in the 2139 and AlSi10Mg alloys, respectively.

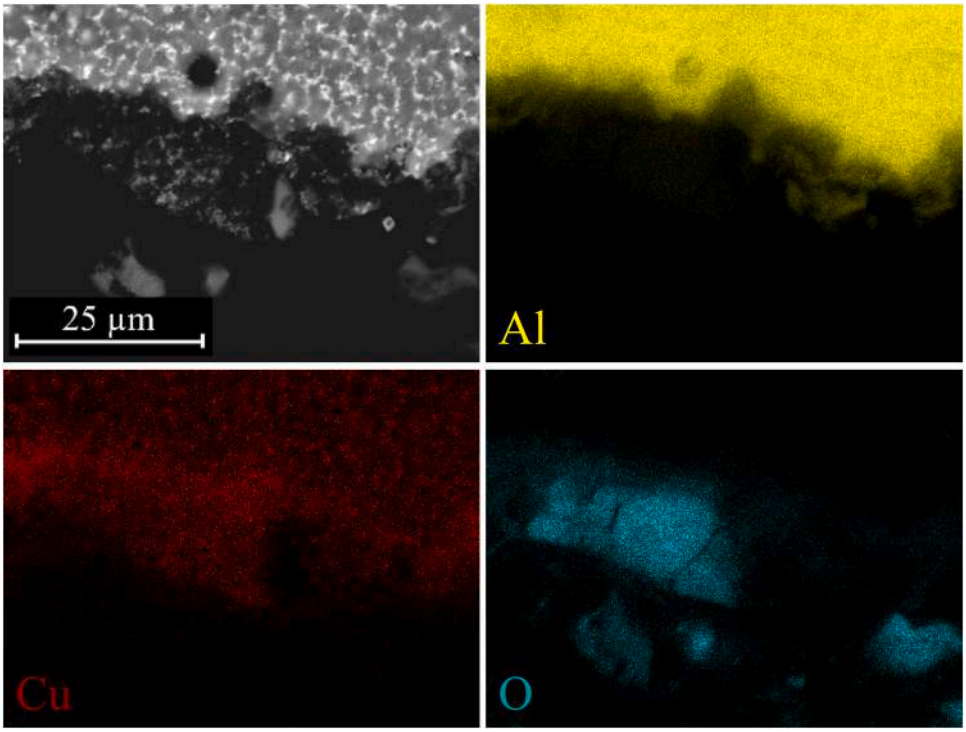

Fig. 9. EDS maps of the corrosion products generated during the susceptibility to intergranular corrosion tests in the AB alloy LPBF 2139.

network inside the crack was observed (Fig. 8e). LPBF AlSi10Mg specimens provided a higher intergranular corrosion resistance than alloy LPBF 2139, with linear attack densities and mass losses one order of magnitude lower (Table 6). This confirmed the results of the electrochemical tests, where a higher corrosion resistance was encountered. However, longer attack depths were documented in LPBF AlSi10Mg alloy, suggesting that this type of corrosion is still not negligible.

To confirm the cathodic effect of the Cu-rich phases identified in the LPBF-processed alloy 2139, a SKPFM was deployed to evaluate the differences in terms of Volta potential between the Al_2Cu network and the surrounding Al matrix, as illustrated in Fig. 7. Schmutz and Frankel [53] reported that the Volta potential measured with the Kelvin probe atomic force microscope vary linearly with open circuit potential measured previously in solution. The results obtained confirm the trend

of OCP and EIS.

By comparing the FESEM (Fig. 10a) and SKPFM (Fig. 10b) views, a clear correlation between the Al_2Cu network and the areas characterized by a high Volta potential is manifest. Volta potential line scans were performed to estimate the potential difference between the Cu-rich network and the surrounding matrix (Fig. 7c). This analysis provided higher differences (+ 140–180 mV) in the correspondence of the edge of the melt pool with respect the center of the melt pool (+ 100–107 mV). These values are comparable with those reported by Wang et al. [54] on an Al-Cu-Mg-Ag alloy, and they are lower than the values reported for a heat treated AA 2024 alloy by Schmutz and Frankel [53] and Leblanc and Frankel [55], that are, respectively, + 280 mV and + 200 mV. The difference between the Volta potential of the Al matrix and Al_2Cu in the LPBF 2139 alloy is higher than the differences observed between the Volta potential of Al matrix and Si in the AlSi10Mg alloy [41] that result + 50 mV for the center of the melt pool and 103 mV in the edge of the melt pool. This difference can justify the deeper intergranular attacks observed.

3.2.2. *Heat-treated specimens*

The microstructural modification induced by the post-processing heat treatments resulted in an increase in terms of OCP in both alloys with respect to the AB specimens. As reported in Table 3, this effect was much more evident for alloy LPBF 2139 than for LPBF AlSi10Mg. The values of OCP of the heat treated LPBF 2139 are like the values obtained for the traditionally hot-rolled alloy AA 2139 T351. The OCPs agree with the values reported by Balbo et al. [36] on the wrought alloy AA 2139 T351 in a similar neutral low chlorides concentration solution.

The EIS spectra of both the LPBF alloys heat treated showed a similar behavior with respect to the corresponding AB (Fig. 11a, b). Even after the heat treatment, the MP specimens showed values of R_2 slightly higher than the NP for the LPBF 2139 T4, whereas the differences between the MP and NP specimens of the LPBF AlSi10Mg T6 are more significant. For this alloy, the time constant at low frequencies was recognizable and the impedance modulus at the lower frequency is about one order of magnitude lower than the correspondent value of the MP specimens (Fig. 11b). It can be hypothesized that the passive film on the alloy is further oxidized during the high temperature annealing in air, increasing in thickness but becoming more porous and, therefore, less protective [47]. Conversely, no differences were observed between the EIS spectra of the MP LPBF AlSi10Mg specimens as a function of the heat treatment (Fig. 10d). Fig. 10c compares the EIS spectra of the LPBF 2139 alloy, AB and HT, with its wrought and heat treated counterpart, AA 2139 T351. The specimens have a similar behavior, as confirmed by the fitting reported in Table 4. However, the low frequency modulus values of the LPBF 2139 T4 specimens are slightly higher than in the AB ones and the rolled AA 2139 T351, as reported in Table 4. This seems to indicate that the T4 heat treatment mildly improves the corrosion resistance of the LPBF 2139 alloy, resulting in higher polarization resistances.

The PD polarization curves (Fig. 12) did not evidence significant variations in the corrosion behavior of the HT specimens of both alloys with respect to the AB condition. The PD polarization curves of the AB and HT specimens with NP surfaces showed active behavior and corrosion current density one order of magnitude higher than their polished counterparts, confirming the lower corrosion resistance of the aluminum passive film formed during LPBF with respect to the air formed one, regardless of the alloy. Nevertheless, whilst the MP T4 2139 alloy maintained a fully active behavior, the MP T6 LPBF AlSi10Mg alloy showed a passive trait characterized by higher anodic currents and lower breakdown potentials, if compared to the corresponding AB specimens (Table 5). This is in accordance with the slightly lower low frequencies modulus values obtained during the EIS tests. An active behavior is shown by the alloy AA 2139 T351, with corrosion current densities comparable to the MP LPBF 2139 AB and slightly higher than the MP LPBF 2139 T4.

The LPBF AlSi10Mg specimens were barely affected by the microstructural changes induced by the heat treatment, resulting in corrosion current density values comparable between AB and T6 specimens. Moreover, the heat-treated 2139 alloy kept providing higher corrosion current densities than AlSi10Mg, confirming the comparatively superior cathodic effect of the copper-rich second phases.

The post-processing heat treatments provided a significant variation in terms of susceptibility to intergranular corrosion and relative morphology of the attack (Table 6). The LPBF 2139 HT specimens were still characterized by selective attacks. However, these no longer followed a clear preferential path (Fig. 13a) as in the AB specimens. This can be correlated to the second phases redistribution occurred during the T4 heat treatment (Fig. 1). In fact, the selective attacks appeared less elongated and no Cu-rich network was encountered, due to its disruption in the T4 state. Nevertheless, some dispersed Al_2Cu particles were still observed in correspondence of the edge of the corrosion products (Fig. 13b, c), in a similar fashion to the Al_2Cu network in the AB specimens. These observations are confirmed by the EDS maps of the

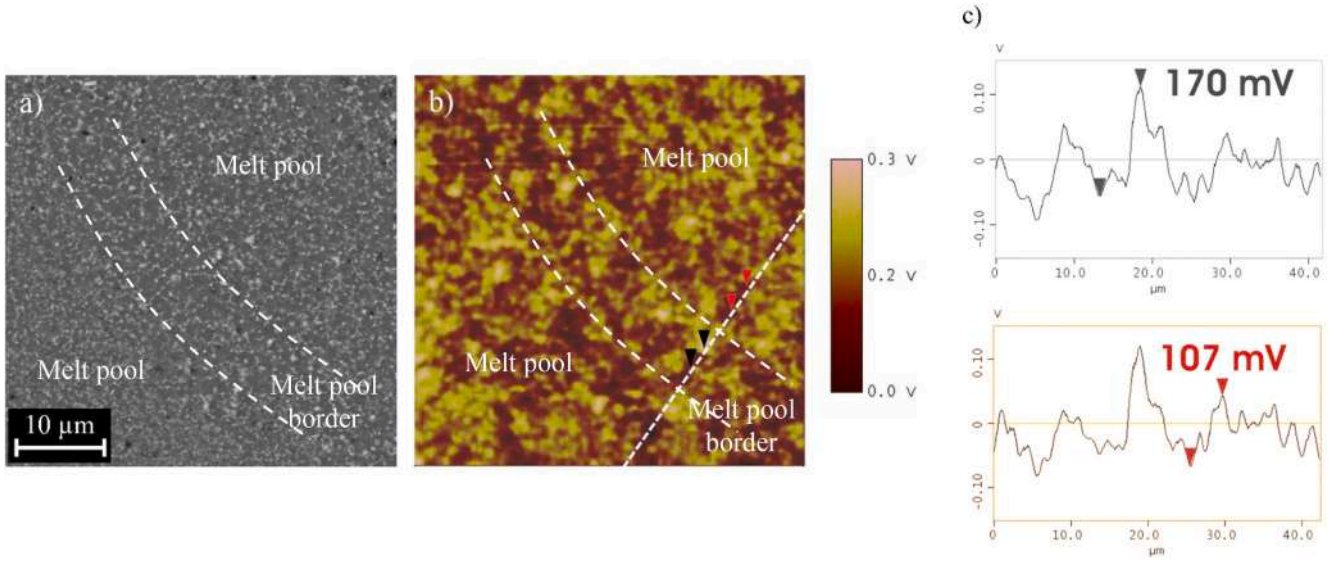

Fig. 10. FESEM micrograph (a) and relative Volta potential map obtained by means of SKPFM (b) in a LPBF-processed alloy 2139 specimen. Volta potential line scan crossing a Cu-rich area and the matrix (c).

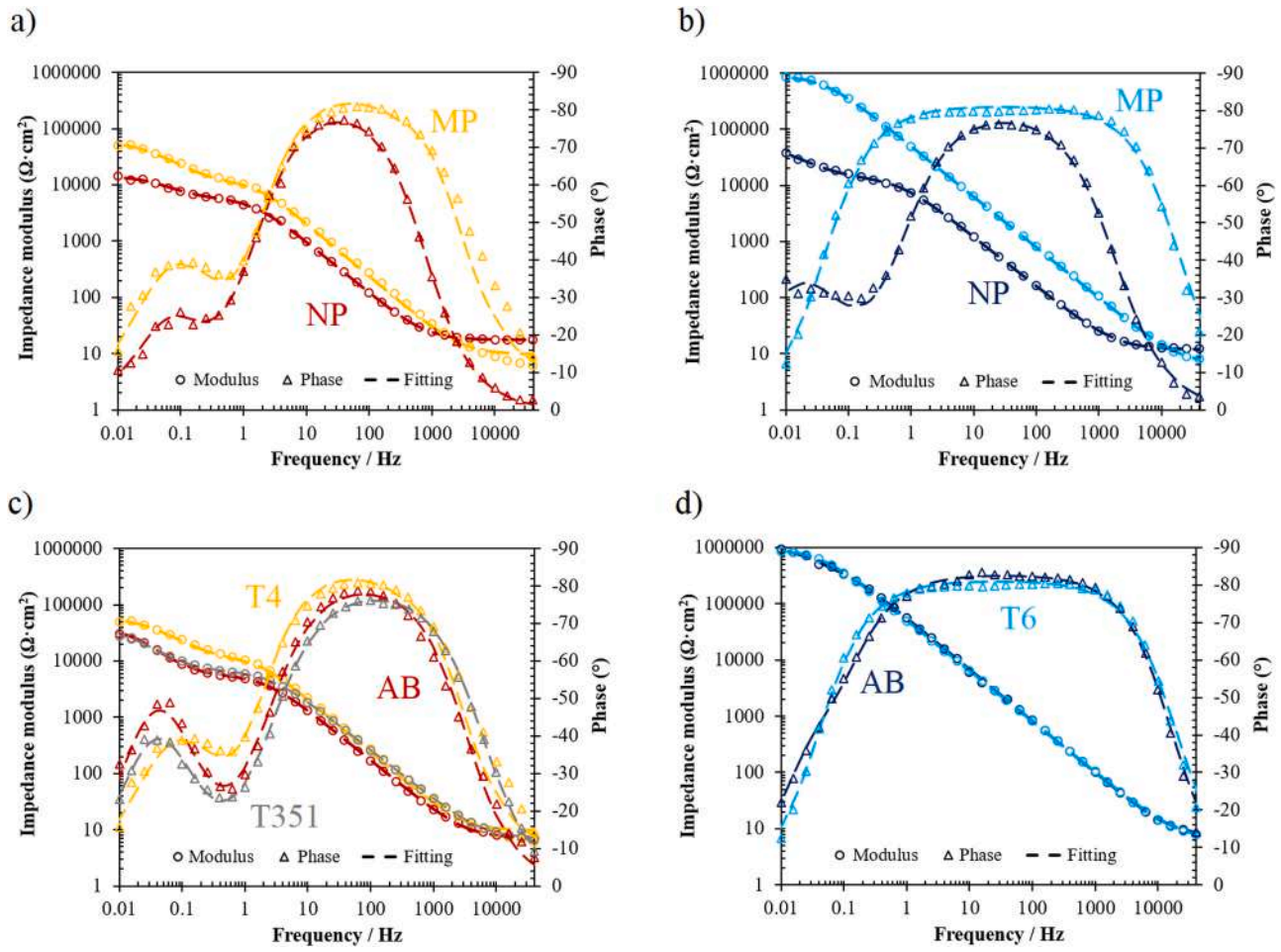

Fig. 11. EIS spectra of LPBF 2139 (a) and LPBF AlSi10Mg (b) heat treated specimens; EIS spectra of LPBF and wrought 2139 (c) and LPBF AlSi10Mg (d) MP specimens.

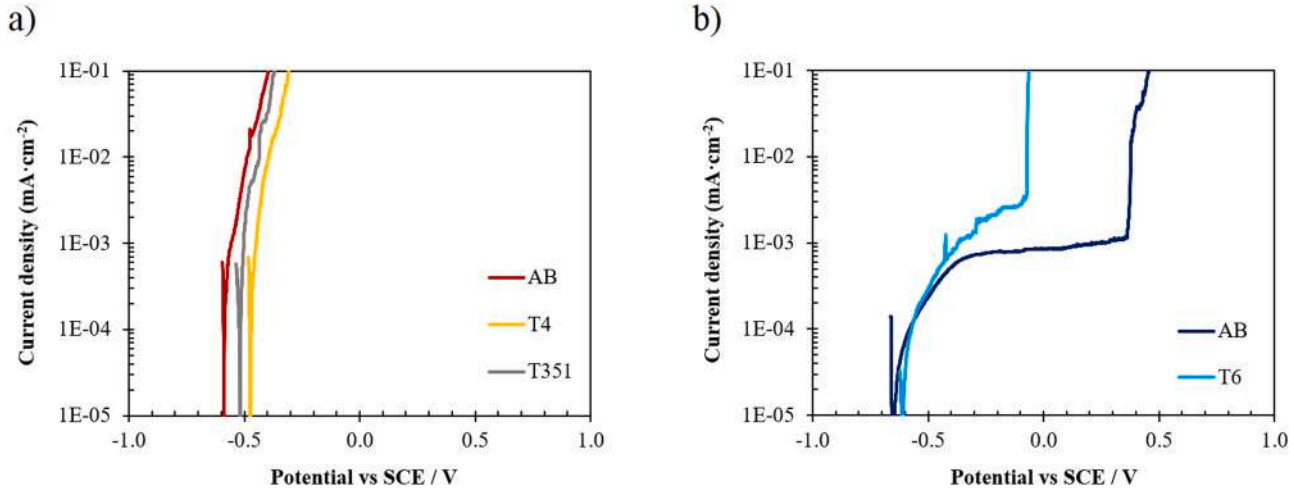

Fig. 12. Potentiodynamic polarization curves of the 2139 (LPBF and hot rolled) (a) and LPBF AlSi10Mg (b) MP specimens.

corrosion products (Fig. 14). In fact, the alloy LPBF 2139 HT did not provide a significant amount of Al in correspondence of these areas, while relevant quantities of Cu and O were found. Thus, confirming the preferential dissolution of the α-Al matrix. These morphological differences resulted in a more homogeneous selective corrosion advancement, leading to weight losses an order of magnitude lower than the as-built specimens. No relevant melt pool or grain dropping was observed.

The rolled AA 2139 T351 alloy showed an intense intergranular attack depending on the grain orientation (maximum in the rolling direction) (Fig. 15a). In this case, the attacks average depth is comparable to the AB LPBF 2139 (Table 6), whereas the mass losses are lower, because the corrosion growth along the direction transversal to the rolling direction is significatively lower. With the traditionally worked AA 2139 alloy, the selective attack propagates along the distribution of

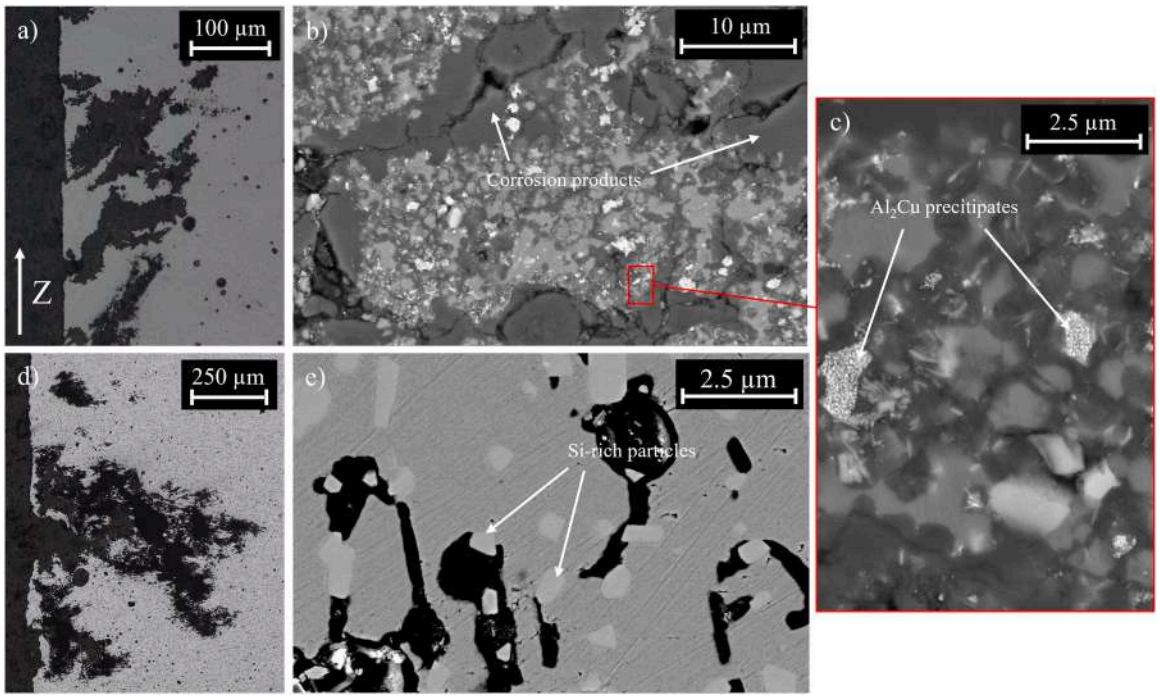

Fig. 13. Morphology of the selective attack at the edge of the T4 alloy 2139 specimen (a), relative propagation (b) and inset highlighting the presence of Al_2Cu (c). Morphology of the selective attack at the edge of the T6 AlSi10Mg specimen (d) and relative propagation (e).

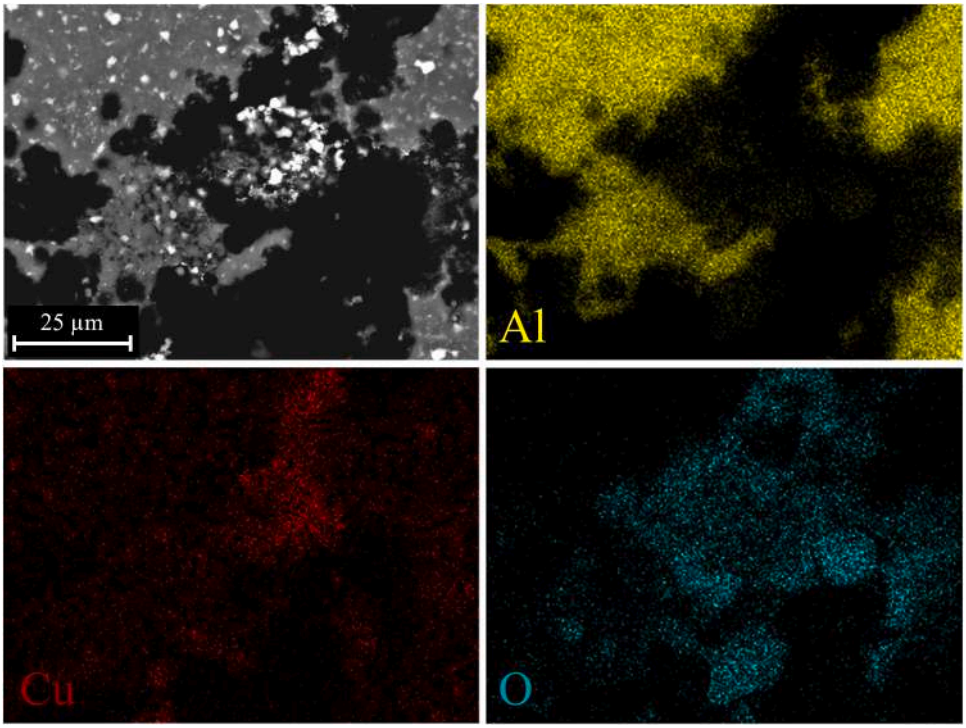

Fig. 14. EDS maps of the corrosion products generated during the susceptibility to intergranular corrosion tests in the T4 alloy 2139.

copper-rich coarse precipitates (Fig. 15b, c).

The T6 heat treatment resulted in a clear variation in the morphologies of the attacks in the AlSi10Mg specimens as well (Fig. 13d). These appeared more similar to the typical morphologies of localized attacks with the occluded cell structure. The relative propagations seemed to be less affected by the presence of the second phase with respect to the T4 2139 alloy (Fig. 13e). Nevertheless, the cathodic effect of the coarse Si-rich particles is still evident, with the preferential dissolution of the α-Al matrix. Even for the AlSi10Mg alloy, the heat treatment induced a reduction in terms of weight loss with respect to AB specimens, although the results were still of the same order of magnitude.

SKPFM analyses were also performed on the T4 2139 alloy specimens, as reported in Fig. 16. The highest Volta potential was found in correspondence of the largest Al_2Cu particles. These were characterized

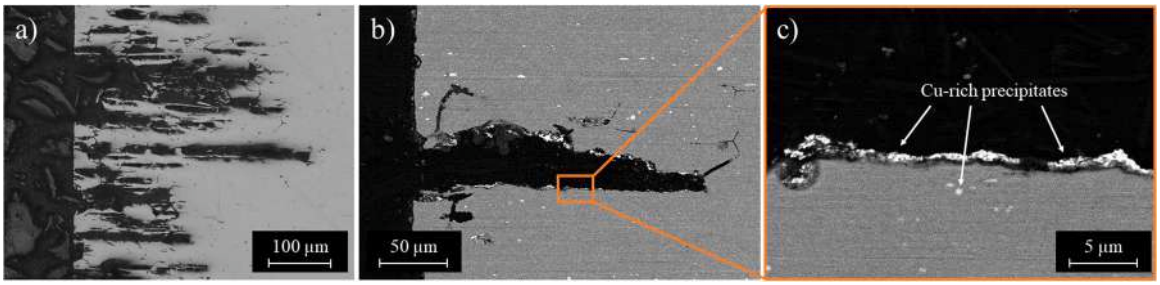

Fig. 15. MO (a) and FESEM (b) low magnification images of the selective attack morphology of the T351 alloy 2139 specimen and inset highlighting the presence of Cu-rich precipitates (c).

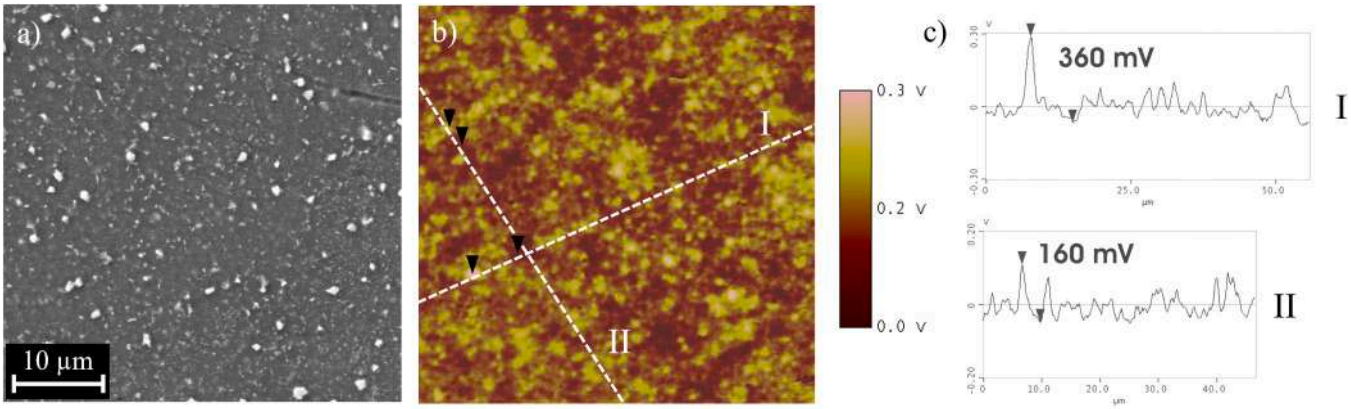

Fig. 16. FESEM micrograph (a) and relative Volta potential map obtained by means of SKPFM (b) in a heat-treated LPBF-processed alloy 2139 specimen. Volta potential line scans crossing a large Cu-rich particle (I) and a smaller Cu-enriched zone (II), respectively (c).

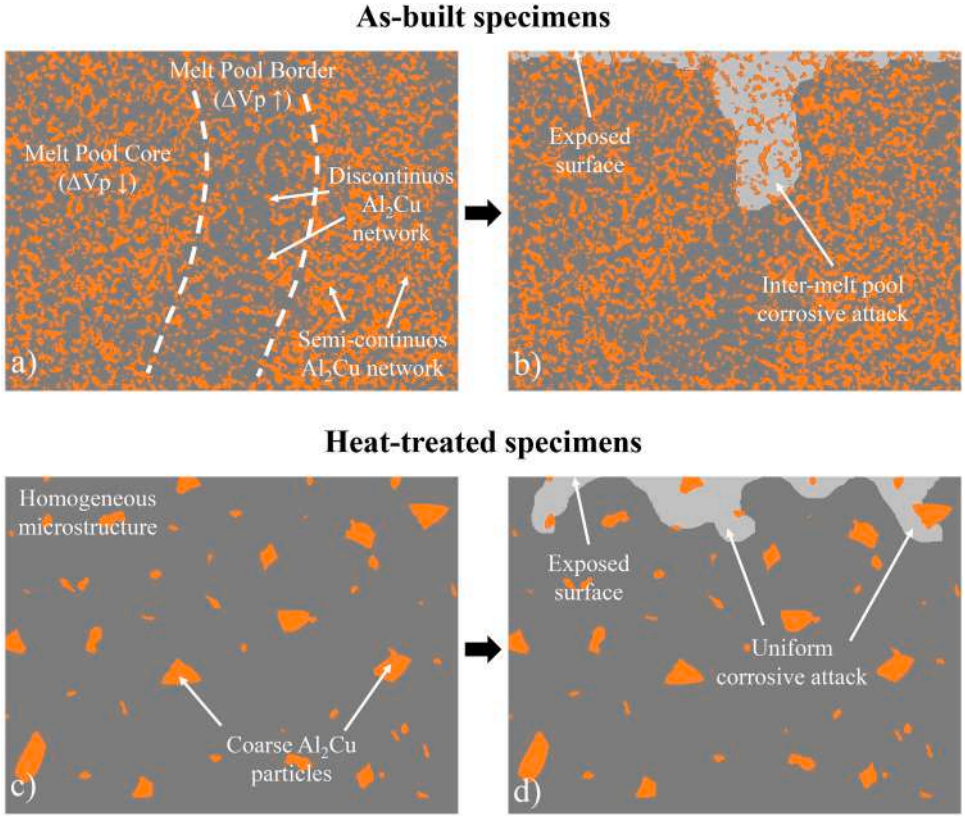

Fig. 17. Schematic representation of the selective corrosion of the AB LPBF 2139 (a,b) and HT LPBF 2139 (c,d).

by a potential difference with the surrounding matrix as high as 360 mV (Fig. 16c, I). This value is significantly higher than the ones measured in the AB condition (Fig. 10). Conversely, the areas characterized by a lack of bulky particles (Fig. 16c, II) provided comparable potential differences (160 mV) with respect to the edge of the melt pool in AB condition.

These data suggest a more intense cathodic effect given by the larger particles, that might promote local corrosion phenomena. Nevertheless, these particles appeared quite sparsely distributed. Therefore, it is possible that a continuously distributed and frequent network of a lower Volta potential difference (AB condition) might induce anyway more conspicuous corrosion phenomena.

3.2.3. Corrosion mechanism

The obtained results underlined the effect of microstructure and precipitates on the selective corrosion of the considered Al-Cu alloy. For the LPBF-processed alloy in AB conditions, a selective corrosion of the edge of the melt pool was observed. The metallographic analysis highlighted a different size distribution of the precipitates between the center and the edge of the melt pool, resulting in higher differences between the Volta potentials of Al matrix and precipitates. These differences are responsible of the observed selective attack. The possible mechanism for the AB LPBF 2139 alloy is shown in Fig. 17a,b.

The cathodic effect of copper precipitates is higher than silicon ones observed in LPBF AlSi0Mg [41], due to the lower overpotential for OER. This leads to a strong alkalinization near the precipitates, destabilizing the passive film. When the aluminum passive film is destroyed, the galvanic effect becomes less important because the main cathodic process becomes hydrogen evolution. The corrosion attacks proceed along the preferential path of the edge of the melt pool, and the attacks are filled of corrosion products that surround the copper-rich precipitates. The heat treatments induce the coalescence of the very fine microstructures produced by the LPBF process, giving α-Al grains with macroprecipitates of Al_2Cu. The melt pool macrostructure is destroyed. The galvanic effect of the second phase is enhanced, but their more homogeneous distribution changes the morphology of the attack from a deep penetrating selective dissolution of the edge of the melt pool in a more uniform attack with corrosion rate one orde of magnitude lower than the untreated specimens (Fig. 17c,d).

4. Conclusions

In this work, the corrosion behavior of an LPBF-processed alloy 2139 was assessed via electrochemical impedance spectroscopy, potentiodynamic and susceptibility to intergranular corrosion tests. The corrosion properties highlighted by this material were correlated to its microstructural/phase composition via FESEM imaging, XRD evaluations and SKPFM maps. The results were compared with similar tests carried out on a commercial hot rolled and heat treated AA 2139 alloy. In addition, a well-established in the LPBF industry benchmark AlSi10Mg alloy was also investigated and comparatively analyzed. The main results obtained can be summarized as follows:

- The LPBF 2139 alloy was characterized by a semi-continuous network of Al_2Cu precipitates, surrounding the α-Al cells. After the T4 heat treatment, this network disappeared in favor of larger Al_2Cu precipitates, thus eliminating the typical melt pool microstructure.
- Both LPBF alloy 2139 and AlSi10Mg provided an active behavior in the as-printed surface condition. Mechanical polishing resulted in a transition from an active to a passive behavior for the AlSi10Mg alloy only. This was correlated to the higher efficiency of the Cu-rich particles in LPBF alloy 2139, as demonstrated via SKPFM mapping. A very similar behavior was observed for the hot rolled AA 2139 T351. Therefore, the corrosion phenomena are predominantly governed by the microstructure/phases in alloy 2139. Conversely, the passive layer quality is the main factor determining the behavior of AlSi10Mg.
- LPBF alloys provided an inter-melt pool corrosion morphology during the susceptibility to intergranular corrosion tests. The weight losses associated with alloy 2139 were an order of magnitude higher than AlSi10Mg alloy.
- In the heat-treated condition, LPBF alloy 2139 kept providing an active behavior during potentiodynamic tests, unlike AlSi10Mg. Nevertheless, the relative mass losses recorded during the susceptibility to intergranular corrosion tests were significantly decreased. Additionally, the inter-melt pool attack morphology disappeared, due to the significant microstructural changes induced by the heat treatment. The mass loss and corrosion rate of the HT LPBF 2139 alloy are significatively lower than the correspondent wrought HT AA 2139. This means that the T4 heat treatment has a positive effect on both hardness and selective corrosion.

Declaration of Competing Interest

The authors declare that they have no known competing financial interests or personal relationships that could have appeared to influence the work reported in this paper.

Data Availability

Data will be made available on request.

Acknowledgements

This research work has been funded by Regione Lombardia (Italy), regional law n° 9/2020, resolution n° 3776/2020.

References

[1] O.H. Laguna, P.F. Lietor, F.J.I. Godino, F.A. Corpas-Iglesias, A review on additive manufacturing and materials for catalytic applications: milestones, key concepts, advances and perspectives, Mater. Des. 208 (2021), 109927.
[2] C. Mandache, Overview of non-destructive evaluation techniques for metal-based additive manufacturing, Mater. Sci. Technol. 35 (2019) 1007–1015.
[3] J. Fiocchi, A. Tuissi, C.A. Biffi, Heat treatment of aluminium alloys produced by laser powder bed fusion: a review, Mater. Des. 204 (2021), 109651.
[4] K. Tsaknopoulos, J. Grubbs, B.C. Sousa, M. Siopis, A. Nardi, D.L. Cote, Evaluation of a laser powder bed fusion designer Al-Mg-Zr-Si alloy for cold spray additive manufacturing, Mater. Des. 222 (2022), 111105.
[5] A. Martínez-García, M. Monzón, R. Paz, Standards for additive manufacturing technologies: structure and impact. Addit Manuf, Elsevier,, 2021, pp. 395–408.
[6] Z. Chen, C. Han, M. Gao, S.Y. Kandukuri, K. Zhou, A review on qualification and certification for metal additive manufacturing, Virtual Phys. Prototyp. 17 (2022) 382–405.
[7] N.T. Aboulkhair, M. Simonelli, L. Parry, I. Ashcroft, C. Tuck, R. Hague, 3D printing of aluminium alloys: additive manufacturing of aluminium alloys using selective laser melting, Prog. Mater. Sci. 106 (2019), 100578.
[8] A. Aversa, G. Marchese, A. Saboori, E. Bassini, D. Manfredi, S. Biamino, D. Ugues, P. Fino, M. Lombardi, New aluminum alloys specifically designed for laser powder bed fusion: a review, Materials 12 (2019) 1007.
[9] L. Brock, I. Ogunsanya, H. Asgari, S. Patel, M. Vlasea, Relative performance of additively manufactured and cast aluminum alloys, J. Mater. Eng. Perform. 30 (2021) 760–782.
[10] L. Zhou, H. Hyer, J. Chang, A. Mehta, T. Huynh, Y. Yang, Y. Sohn, Microstructure, mechanical performance, and corrosion behavior of additively manufactured aluminum alloy 5083 with 0.7 and 1.0 wt% Zr addition, Mater. Sci. Eng.: A 823 (2021), 141679.
[11] R.L. Bradford, L. Cao, D. Klosterman, F. Herman, L. Forman, C. Browning, A metal–metal powder formulation approach for laser additive manufacturing of difficult-to-print high-strength aluminum alloys, Mater. Lett. 300 (2021), 130113.
[12] H. Qin, Q. Dong, V. Fallah, M.R. Daymond, Rapid solidification and non-equilibrium phase constitution in laser powder bed fusion (LPBF) of AlSi10Mg alloy: Analysis of nano-precipitates, eutectic phases, and hardness evolution, Metall. Mater. Trans. A 51 (2020) 448–466.
[13] J.G.S. Macías, T. Douillard, L. Zhao, E. Maire, G. Pyka, A. Simar, Influence on microstructure, strength and ductility of build platform temperature during laser powder bed fusion of AlSi10Mg, Acta Mater. 201 (2020) 231–243.
[14] P. van Cauwenbergh, V. Samaee, L. Thijs, J. Nejezchlebová, P. Sedlak, A. Iveković, D. Schryvers, B. van Hooreweder, K. Vanmeensel, Unravelling the multi-scale structure–property relationship of laser powder bed fusion processed and heat-treated AlSi10Mg, Sci. Rep. 11 (2021) 1–15.

[15] A. Ghasemi, E. Fereiduni, M. Balbaa, M. Elbestawi, S. Habibi, Unraveling the low thermal conductivity of the LPBF fabricated pure Al, AlSi12, and AlSi10Mg alloys through substrate preheating, Addit. Manuf. 59 (2022), 103148.
[16] F. Li, T. Zhang, Y. Wu, C. Chen, K. Zhou, Microstructure, mechanical properties, and crack formation of aluminum alloy 6063 produced via laser powder bed fusion, J. Mater. Sci. (2022) 1–15.
[17] G. Sander, J. Tan, P. Balan, O. Gharbi, D.R. Feenstra, L. Singer, S. Thomas, R. G. Kelly, J.R. Scully, N. Birbilis, Corrosion of additively manufactured alloys: a review, Corrosion 74 (2018) 1318–1350.
[18] R. Baitimerov, P. Lykov, D. Zherebtsov, L. Radionova, A. Shultc, K.G. Prashanth, Influence of powder characteristics on processability of AlSi12 alloy fabricated by selective laser melting, Materials 11 (2018) 742.
[19] A. Aversa, M. Lorusso, F. Trevisan, E.P. Ambrosio, F. Calignano, D. Manfredi, S. Biamino, P. Fino, M. Lombardi, M. Pavese, Effect of process and post-process conditions on the mechanical properties of an A357 alloy produced via laser powder bed fusion, Met. (Basel) 7 (2017) 68.
[20] P. Mair, V.S. Goettgens, T. Rainer, N. Weinberger, I. Letofsky-Papst, S. Mitsche, G. Leichtfried, Laser powder bed fusion of nano-CaB6 decorated 2024 aluminum alloy, J. Alloy. Compd. 863 (2021), 158714.
[21] E. Maleki, O. Unal, M. Bandini, M. Guagliano, S. Bagherifard, Individual and synergistic effects of thermal and mechanical surface post-treatments on wear and corrosion behavior of laser powder bed fusion AlSi10Mg, J. Mater. Process Technol. 302 (2022), 117479.
[22] M. Cabrini, S. Lorenzi, T. Pastore, C. Testa, D. Manfredi, G. Cattano, F. Calignano, Corrosion resistance in chloride solution of the AlSi10Mg alloy obtained by means of LPBF, Surf. Interface Anal. 51 (2019) 1159–1164.
[23] E. Maleki, S. Bagherifard, O. Unal, F. Sabouri, M. Bandini, M. Guagliano, Effects of different mechanical and chemical surface post-treatments on mechanical and surface properties of as-built laser powder bed fusion AlSi10Mg, Surf. Coat. Technol. 439 (2022), 128391.
[24] A. Leon, A. Shirizly, E. Aghion, Corrosion behavior of AlSi10Mg alloy produced by additive manufacturing (AM) vs. its counterpart gravity cast alloy, Met. (Basel) 6 (2016) 148.
[25] P. Fathi, M. Mohammadi, X. Duan, A.M. Nasiri, A comparative study on corrosion and microstructure of direct metal laser sintered AlSi10Mg_200C and die cast A360. 1 aluminum, J. Mater. Process Technol. 259 (2018) 1–14.
[26] J.E. Hatch, Aluminum: Properties and Physical Metallurgy (Aluminum Association Inc. and ASM International, (1984).
[27] F. Bosio, A. Aversa, M. Lorusso, S. Marola, D. Gianoglio, L. Battezzati, P. Fino, D. Manfredi, M. Lombardi, A time-saving and cost-effective method to process alloys by Laser Powder Bed Fusion, Mater. Des. 181 (2019), 107949.
[28] M. Avateffazeli, P.E. Carrion, B. Shachi-Amirkhiz, H. Pirgazi, M. Mohammadi, N. Shamsaei, M. Haghshenas, Correlation between tensile properties, microstructure, and processing routes of an Al–Cu–Mg–Ag–TiB2 (A205) alloy: Additive manufacturing and casting, Mater. Sci. Eng.: A 841 (2022), 142989.
[29] S. Bai, Z. Liu, X. Zhou, P. Xia, S. Zeng, Mg-controlled formation of Mg–Ag co-clusters in initial aged Al–Cu–Mg–Ag alloys, J. Alloy. Compd. 602 (2014) 193–198.
[30] C. Brice, R. Shenoy, M. Kral, K. Buchannan, Precipitation behavior of aluminum alloy 2139 fabricated using additive manufacturing, Mater. Sci. Eng.: A 648 (2015) 9–14.
[31] C.A. Brice, W.A. Tayon, J.A. Newman, M. v Kral, C. Bishop, A. Sokolova, Effect of compositional changes on microstructure in additively manufactured aluminum alloy 2139, Mater. Charact. 143 (2018) 50–58.
[32] J. Elambasseril, M.J. Benoit, S. Zhu, M.A. Easton, E. Lui, C.A. Brice, M. Qian, M. Brandt, Effect of process parameters and grain refinement on hot tearing susceptibility of high strength aluminum alloy 2139 in laser powder bed fusion, Prog. Addit. Manuf. (2022) 1–15.
[33] A.S. Román, C.M. Méndez, C.A. Gervasi, R.B. Rebak, A.E. Ares, Corrosion Resistance of Aluminum-Copper Alloys with Different Grain Structures, J. Mater. Eng. Perform. 30 (2021) 131–144.
[34] W.R. Osório, L.C. Peixoto, L.R. Garcia, A. Garcia, Corrosion behavior of hypoeutectic Al-Cu alloys in H_2SO_4 and NaCl solutions, Acta Metall. Sin. (Engl. Lett.) 22 (2009) 241–246.
[35] A. Banu, M. Marcu, O. Radovici, C. Pirvu, M. Vasilescu, Electrodissolution studies of three aluminum alloys in acid, neutral and alkaline solutions, Rev. Roum. De. Chim. 51 (2006) 193.
[36] A. Balbo, A. Frignani, V. Grassi, F. Zucchi, Electrochemical behaviour of AA2198 and AA2139 in neutral solutions, Mater. Corros. 66 (2015) 796–802.
[37] F. Trevisan, F. Calignano, M. Lorusso, J. Pakkanen, A. Aversa, E.P. Ambrosio, M. Lombardi, P. Fino, D. Manfredi, On the selective laser melting (SLM) of the AlSi10Mg alloy: process, microstructure, and mechanical properties, Materials 10 (2017) 76.
[38] U. Patakham, A. Palasay, P. Wila, R. Tongsri, MPB characteristics and Si morphologies on mechanical properties and fracture behavior of SLM AlSi10Mg, Mater. Sci. Eng.: A 821 (2021), 141602.
[39] D. Buchbinder, W. Meiners, K. Wissenbach, R. Poprawe, Selective laser melting of aluminum die-cast alloy—Correlations between process parameters, solidification conditions, and resulting mechanical properties, J. Laser Appl. 27 (2015), S29205.
[40] O. Cavusoglu, A.G. Leacock, H. Gurun, A. Gural, Strain-rate-dependent tensile characteristics of AA2139-T351 aluminum alloy, (2017) doi:10.17222/mit.2016.009.
[41] M. Cabrini, S. Lorenzi, T. Pastore, C. Testa, D. Manfredi, M. Lorusso, F. Calignano, M. Pavese, F. Andreatta, Corrosion behavior of AlSi10Mg alloy produced by laser powder bed fusion under chloride exposure, Corros. Sci. 152 (2019) 101–108.
[42] E. Mc Cafferty, Sequence of steps in the pitting of aluminum by chloride ions, Corros. Sci. 45 (2003) 1421–1438.
[43] Y. Liew, C. Örnek, J. Pan, D. Thierry, S. Wijesinghe, D.J. Blackwood, Towards understanding micro-galvanic activities in localised corrosion of AA2099 aluminium alloy, Electro Acta 392 (2021), 139005.
[44] J.R. Scully, T.O. Knight, R.G. Buchheit, D.E. Peebles, Electrochemical characteristics of the Al2Cu, Al3Ta and Al3Zr intermetallic phases and their relevancy to the localized corrosion of Al alloys, Corros. Sci. 35 (1993) 185–195.
[45] N. Birbilis, R.G. Buchheit, Electrochemical Characteristics of Intermetallic Phases in Aluminum Alloys: An Experimental Survey and Discussion, J. Electrochem. Soc. 152 (2005) B140.
[46] J.A. Moreto, C.E.B. Marino, W.W. Bose Filho, L.A. da Rocha, J.C.S. Fernandes, SVET, SKP and EIS study of the corrosion behaviour of high strength Al and Al–Li alloys used in aircraft fabrication, Corros. Sci. 84 (2014) 30–41.
[47] M. Cabrini, S. Lorenzi, T. Pastore, S. Pellegrini, E.P. Ambrosio, F. Calignano, D. Manfredi, M. Pavese, P. Fino, Effect of heat treatment on corrosion resistance of DMLS AlSi10Mg alloy, Electro Acta 206 (2016) 346–355.
[48] M.E. Orazem, B. Tribollet, Electrochemical impedance spectroscopy, John Wiley & Sons, Inc., 2008, https://doi.org/10.1002/9780470381588.
[49] M. Cabrini, S. Lorenzi, C. Testa, D. Manfredi, M. Lombardi, A. Aversa, F. Andreatta, L. Fedrizzi, Y. Dekhtyar, H. Sorokins, Effect of heat treatment on microstructure and selective corrosion of LPBF-AlSi10Mg by means of SKPFM and exo-electron emission, Materials 14 (2021) 5602.
[50] R.I. Revilla, J. Liang, S. Godet, I. de Graeve, Local corrosion behavior of additive manufactured AlSiMg alloy assessed by SEM and SKPFM, J. Electrochem Soc. 164 (2016) C27.
[51] T. Rubben, R.I. Revilla, I. De Graeve, Influence of heat treatments on the corrosion mechanism of additive manufactured AlSi10Mg, Corros. Sci. 147 (2019) 406–415.
[52] R.I. Revilla, I. De Graeve, Influence of Si content on the microstructure and corrosion behavior of additive manufactured Al-Si alloys, J. Electrochem. Soc. 165 (2018) C926.
[53] P. Schmutz, G.S. Frankel, Characterization of AA2024–T3 by scanning kelvin probe force microscopy, J. Electrochem. Soc. 145 (1998) 2285.
[54] J. Wang, Z. Liu, S. Bai, J. Cao, J. Zhao, D. Zeng, Combined effect of Ag and Mg additions on localized corrosion behavior of Al-Cu alloys with high Cu content, J. Mater. Eng. Perform. 29 (2020) 6108–6117.
[55] P. Leblanc, G.S. Frankel, A study of corrosion and pitting initiation of AA2024-T3 using atomic force microscopy, J. Electrochem. Soc. 149 (2002) B239.